Processing of x-ray images obtained with laser-betatron radiation generated using Gemini

Contact: dan.symes@stfc.ac.uk

D. R. Symes, S. Botchway, D Rusby, P. S. Foster, S. Gratton
Central Laser Facility, STFC Rutherford Appleton Laboratory, Didcot OX11 0QX, UK

J. M. Cole, J. C. Wood, K. Poder, S. Alatabi, C Kamperidis, N. C. Lopes, S. P. D. Mangles, Z. Najmudin
The John Adams Institute for Accelerator Science, Blackett Laboratory, Imperial College London, London SW7 2AZ

J Sanderson, M Sandholzer, H Westerberg, DP Norris
MRC Harwell Institute, Harwell Campus, Oxfordshire, OX11 0RD, UK

S Johnson, Z Szoke-Kovacs, L Teboul
The Mary Lyon Centre, MRC Harwell Institute, Harwell Campus, Oxfordshire, OX11 0RD, UK

M De Lazzari, JM Thompson, MA Hill
CRUK/MRC Oxford Institute for Radiation Oncology, University of Oxford, Gray Laboratories, ORCRB Roosevelt Drive, Oxford OX3 7DQ, UK

O Kononenko, CAJ Palmer
Deutsches Elektronen-Synchrotron DESY Notkestr. 85, 22607 Hamburg, Germany

JR Warwick, G Sarri
School of Mathematics and Physics, Queen's University Belfast, University Road, BT7 1NN, UK

1 Introduction

X-rays generated through betatron oscillations of electrons in laser wakefield accelerators have ideal properties for biological imaging. In recent years, experiments on Gemini have increased the flux and critical energy of betatron x-rays into the 10s keV regime that is needed to penetrate cm-scale objects such as bone samples, mouse embryos, and soft tissue biopsies. To translate these proof of principle demonstrations into a resource for preclinical and clinical imaging, and biological research, effort is needed to address the stability of the plasma accelerator and thereby the quality of x-ray radiographs produced. Many groups are making progress on this front with robust machine design [1] and more consistent injection schemes into the laser wakefield [2, 3, 4]. Until this is achieved, data analysis will be complicated by fluctuations in x-ray profile, spectrum and brightness. We recently reported tomography of an ex vivo mouse embryo [5], representing an important step in our capability for imaging complicated organisms with direct relevance for studies of human disease. In this report, we discuss the image quality and processing steps taken to obtain this tomographic reconstruction.

2 Method

The arrangement for x-ray imaging is shown in figure 1(a). Gemini was operated with a laser power of 120 – 240 TW (6 – 12 J in 50 fs) focussed through a helium filled gas cell using an $f/40$ parabolic mirror. A thin plastic tape drive terminated the laser and electrons were deflected off-axis using a strong permanent magnet (∼1 T). For high magnification imaging an additional magnet was inserted to avoid striking the sample directly with the electron beam. The sample was imaged by point projection to an x-ray CCD detector with the magnification determined by the source-sample-detector distances. Samples were placed in three locations indicated in the layout diagram in figure 1(a): position A was closest to the source and had a magnification $M = 10$ and field of view $FOV = 2.6 \times 2.6\,\mathrm{mm}^2$, B was at the rear of the vacuum chamber with $M = 2.5$ and $FOV = 10.4 \times 10.4\,\mathrm{mm}^2$ and C was directly in front of the x-ray camera ($M = 1$) so gives the largest field of view $FOV = 26.6 \times 26.6\,\mathrm{mm}^2$, but can only provide absorption contrast. X-ray images were recorded using a 150 μm thick structured caesium iodide scintillator fibre-coupled CCD camera with 2048×2048 pixels, each of size 13.5×13.5 μm, located at 3.6 m from the gas cell. Flat field and dark field images were recorded for background subtraction.

Under optimum conditions the beam contained 2.2×10^{10} photons above 5 keV with a critical energy of 20 keV. This corresponds to a peak beam brightness in excess of 10^{24} photons/s/mm^2/mrad^2/0.1%BW assuming an x-ray pulse duration of order 10 fs [6]. The spectrum was recorded simultaneously with sample imaging by placing filters in the corners of the detector. X-ray imaging resolution was determined by taking a radiograph of a JIMA RT RC-02 test target [jima.jp] placed at position A in which 3 μm features are resolved (figure 1(c)). Calculations from the x-ray beam and plasma properties [5] suggest that the x-ray source size was 1μm, meaning the imaging resolution was limited by the scintillator properties of the fibre-coupled hard x-ray camera [7]. At positions B & C a larger gold target was used with 10 μm features which were clearly resolved (figure

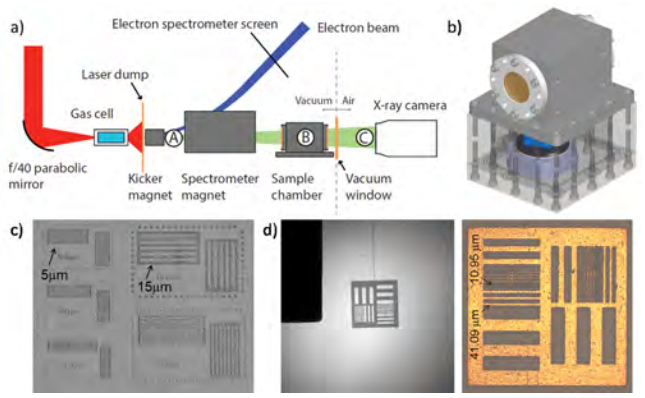

Figure 1: (a) Schematic of the laser-betatron imaging arrangement. (b) Chamber used to house the sample when placed inside the main vacuum chamber. (c) JIMA RT-RC-02 resolution grid imaged at position A. (d) Resolution grid with minimum feature size of 10 μm imaged at position B.

1(d)). The beam divergence was ∼10 mrad full-width-half-maximum, so it was well matched to the camera chip area.

A 14.5 days post-coitum (d.p.c.) mouse embryo of height 10 mm, stained with potassium tri-iodide (Lugol), was embedded in agarose in a 12 mm diameter plastic tube. This was centred on a positioning stage inside an aluminium sample chamber (see figure 1(b)) that was maintained at atmospheric pressure inside the main vacuum chamber. Two 12 μm aluminium foils, added to protect the polyimide windows of the sample chamber, filtered x-ray radiation below 5 keV. Tomographic imaging was conducted by rotating the mouse embryo through 180 degrees in 0.5 degree steps.

3 Results

To produce a tomographic image from the Gemini dataset, first the image quality must be improved through a processing routine, then a reconstruction technique is used to convert the 360 projections into a 3D visualisation of the sample. This is a common procedure for users of commercial x-ray machines and synchrotron facilities, and efforts have been made to standardise software platforms [8] and to provide collaborative support to the tomography community [ccpi.ac.uk]. Some of these methods can be directly applied to laser-betatron x-ray images, but attention needs to be paid to causes of noise and imperfections that are specific to this source. The main difference from conventional sources is the shot-to-shot variation in x-ray brightness and profile. This can be seen by the five typical images shown in figure 2.

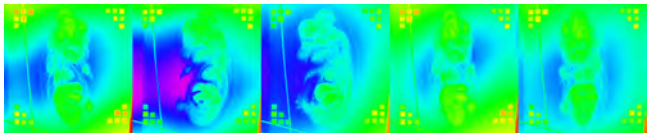

Figure 2: Typical raw images obtained with Gemini laser-betatron source.

3.1 Image processing

Images of the embryo acquired with a single x-ray pulse were recorded with the sample chamber in position B ($M = 2.5$) where the sample fits well onto the detector providing clear imaging of the whole body. The raw data are affected by noise, beamline imperfections, and variations in the pointing and intensity profile of the x-ray beam. An example image as recorded on the x-ray CCD is shown in figure 3(a). A three-step image processing treatment was applied, consisting of background subtraction, correction of abnormally bright or dark pixels and ionisation traces in the detector, and non-local denoising. By averaging 20 images with no sample present, a reference flat field was acquired to determine non-uniformities arising from elements of the beamline, such as windows and foils, and the x-ray detector. This background signal was subtracted from the data. Micron-scale fluctuations in the x-ray source position were removed by tracking the position of the crossing point of the reference wires. By fitting a quadratic surface to the peak of the cross-correlation function of each image to the initial image, it was possible to measure and correct this offset to sub-pixel accuracy.

Figure 3(b) indicates the presence of hot and cold pixels across the image. Hot pixels are produced by high energy photons arising from the tail of the betatron spectrum; bremsstrahlung radiation from the deflected electron beam striking objects in the beamline; and external sources (e.g. cosmic radiation). The number of these photons is low compared to the flux at the peak of the betatron spectrum at $\sim$ 20 keV and they interact only weakly with the detector, but they cause groups of pixels to have abnormally high signal values. Energetic particles impacting the scintillator and CCD chip can also produce hot pixel neighbourhoods or bright lines. Cold pixels are typically a result of an imperfect flat field subtraction. For example, a hexagonal pattern is visible in the raw image because of the fibre coupling of the scintillator to the CCD chip. In some regions there is a remnant of this pattern in the background corrected image. These outlying pixels are removed using a selective median filter resulting in the image shown in figure 3(c).

The majority of the remaining noise comes from Poisson photon noise at the level of several per cent of the signal. While the signal to noise ratio (SNR) can be improved by integrating multiple images, this has the disadvantage of increasing acquisition time. Therefore, to improve single-image SNR we used a non-local-denoising

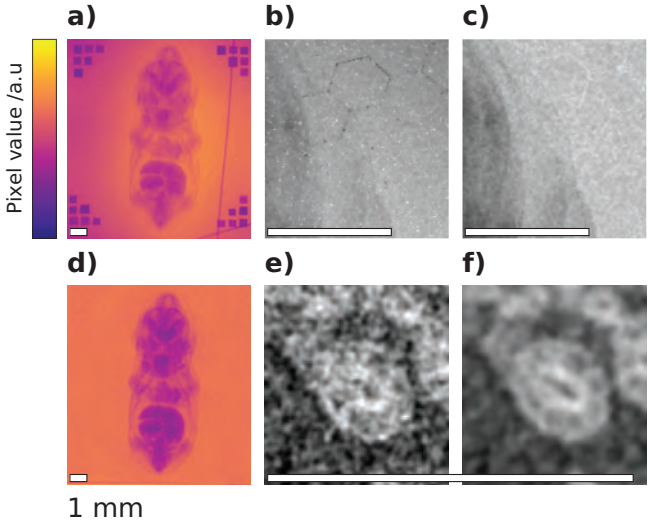

Figure 3: (a) Raw image of mouse embryo detected by the x-ray CCD, wires are placed as fiducials for tomographic reconstruction. (b) Region of image showing hot and cold pixels and (c) the result of applying a selective median filter. (d) Processed version of the image in (a). (e) Zoomed region showing remaining noise and (f) the result of applying a non-local-denoising technique.

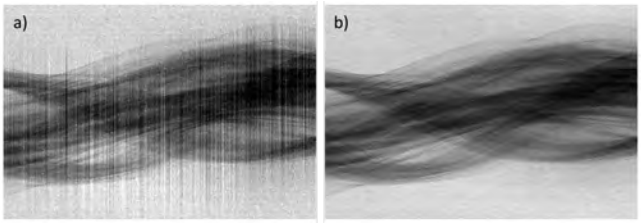

Figure 4: Removal of x-ray beam spectral fluctuations using sinogram.

(NLD) technique, considered the best option for preserving edge definition [9]. This method corrects the intensity of each pixel in the image by defining a pixel neighbourhood (typically a rectangle of pixels around the pixel of interest) and measuring the difference between this and other neighbourhoods in the image or in a near fraction of the image. By averaging the pixel of interest with the central pixels of the most similar neighbourhoods using the similarity as a weight for the average, it is possible to strongly reduce the Poisson noise. Here we have used an implementation of the original non-local denoising algorithm [9] in which each of the pixel neighbourhoods is compared with every possible neighbourhood of the same shape in the image. A threshold is defined that limits the neighbourhood differences that can be tolerated in the average. A trial procedure is then used to find the optimal value of this threshold. This NLD method is computationally intensive, but removes noise without compromising image resolution. For these data we used neighbourhoods of 11×11 pixels. The effect can be seen

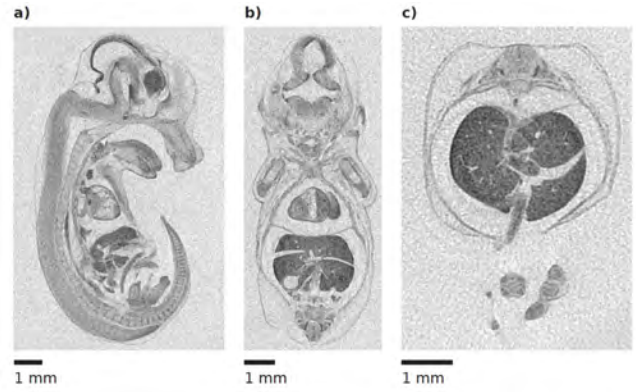

Figure 5: Slices taken through the tomographic reconstruction of the 14.5 d.p.c. mouse embyro in the (a) sagittal (b) coronal and (c) transverse planes.

Figure 6: Volume rendering of the 3D tomographic reconstruction rendered with the Drishti software. Isosurfaces of electron density are shown allowing the visualisation of particular organs.

by comparing the zoomed section of the image displayed in figure 3(e) and (f). On average along an image, the statistical improvement achieved with NLD is normally equivalent to adding 10 to 20 similar images. The final image obtained following this procedure is shown in 3(d).

3.2 Tomographic x-ray imaging

Reconstruction was carried out using a filtered back-projection technique (FBP). This is a very common approach because it is simple, fast and robust. As part of the procedure, a sinogram is generated and further processing can take place at this stage [8, 10]. For example, fluctuations in x-ray transmission caused by changes in spectrum can be corrected as shown in figure 4. Figure 5 displays (a) sagittal, (b) coronal and (c) transverse slices through the tomographic reconstruction. The images exhibit good contrast and SNR with the internal organs, particularly the liver, well defined.

As a method to visualise particular objects we used the Drishti volume renderer to generate 3D representations of the reconstruction and then created iso-surfaces of electron density. This is shown in figure 6 and allows us to step through the reconstruction from the light outer layers of skin and whiskers through to the dense skeletal features, liver and kidneys.

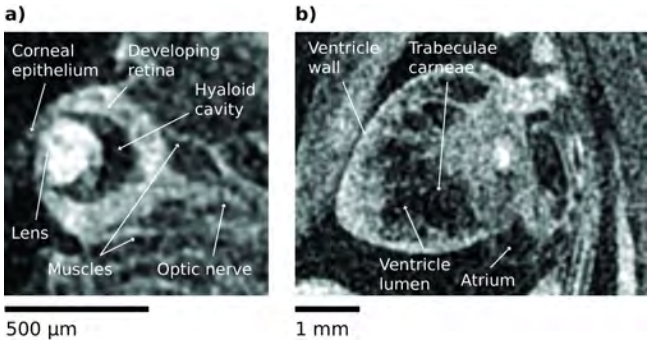

Figure 7: Enlarged sections of the tomographic data showing the structure of (a) the eye and b) the heart. (Note the colourmap is reversed compared to figure 5)

We highlight the good resolution by studying two small features in the embryo in figure 7. Examination of the eye (figure 7(a)) reveals obvious structure, with the forming lens and overlying corneal epithelium clearly imaged, in front of the hyaloid cavity. The developing retina is evident as a ~ 100 μm thick layer and the optic nerve and the ocular muscles are also resolved. Although fine structures such as the pigmented epithelial layer are not resolved, nor are they resolved by standard benchtop *mu*CT machines. Imaging of the heart (figure 7(b)) again resolves substantial structure. At the gross level the ventricles and atria are well resolved, with thicker and thinner regions of the ventricle wall clearly evident. Moreover fine structures, such as the developing trabeculae carneae within the ventricle are resolved.

4 Conclusion

The development of laser wakefield accelerators as x-ray sources for a wide range of applications is a key objective for the CLF and our user community. We have demonstrated high quality biological imaging using laser-betatron radiation. Currently the resolution is detector-limited and this needs to be addressed with further experimental campaigns and detector development. The stability of the accelerator will improve as new facilities come on-line with more reliable laser and target performance. Engagement with existing communities with expertise in tomographic imaging has started and will aid the exploitation of these unique sources for applied science.

5 Ethical information

Mice were produced and housed in the Mary Lyon Centre, MRC Harwell Institute, under specific opportunistic pathogen-free (SOPF) conditions. Individually ventilated cages adhering to environmental conditions as outlined in the Home Office Code of Practice were used. All animal studies were licensed by the Home Office under the Animals (Scientific Procedures) Act 1986 Amendment Regulations 2012 (SI 4/2012/3039), UK, and approved by the Institutional Ethical Review Committee.

6 Acknowledgements

This research was supported by the Science and Technology Facilities Council (ST/J002062/1, ST/P000835/1), the National Institute for Health (Grant U42OD011174), a Medical Research Council IMPC Strategic award to L.T. (53658), an award from the Medical Research Council to D.P.N. (MC_U142670370) and funding from Medical Research Council Strategic Partnership (MC-PC-12004) for the CRUK/MRC Institute for Radiation Oncology. G.S. and J.R.W. acknowledge support from the EPSRC (grant No: EP/P010059/1 and EP/N027175/1). The authors are grateful to the Central Laser Facility staff for assistance during the experiment. The image used in figure 5(a) has been reproduced from reference [5], https://doi.org/10.1073/pnas.1802314115, which was published under the CC BY-NC-ND license.

References

[1] N. Delbos et al. LUX – A laser–plasma driven undulator beamline. *Nuclear Instruments and Methods in Physics Research, Section A: Accelerators, Spectrometers, Detectors and Associated Equipment* **909,** (Nov. 2018), pp. 318–322. eprint: 1801.07651.

[2] J. Faure et al. Controlled injection and acceleration of electrons in plasma wakefields by colliding laser pulses. *Nature* **444,** 7120 (2006), pp. 737–739.

[3] C. McGuffey et al. Ionization induced trapping in a laser wakefield accelerator. *Physical Review Letters* **104,** 2 (2010), pp. 1–4.

[4] M. Tzoufras et al. Improving the self-guiding of an ultraintense laser by tailoring its longitudinal profile. *Physical Review Letters* **113,** 24 (2014), pp. 1–5.

[5] J. M. Cole et al. High-resolution μCT of a mouse embryo using a compact laser-driven X-ray betatron source. *Proceedings of the National Academy of Sciences of the United States of America* **115,** 25 (June 2018), pp. 6335–6340.

[6] J. Wenz et al. Quantitative X-ray phase-contrast microtomography from a compact laser-driven betatron source. *Nature Communications* **6,** May (2015), pp. 1–6.

[7] J. C. Larsson, U. Lundström, and H. M. Hertz. Characterization of scintillator-based detectors for few-ten-keV high-spatial-resolution x-ray imaging. en. *Medical Physics* **43,** 6 (June 2016), pp. 2731–2740.

[8] R. C. Atwood et al. A high-throughput system for high-quality tomographic reconstruction of large datasets at diamond light source. *Philosophical Transactions of the Royal Society A: Mathematical, Physical and Engineering Sciences* **373,** 2043 (June 2015).

[9] A. Buades, B. Coll, and J. M. Morel. A review of image denoising algorithms, with a new one. *Multiscale Modeling and Simulation* **4,** (2005), pp. 490–530.

[10] J. M. Cole. Diagnosis and application of laser wakefield accelerators. *Dissertation. Imperial College London* (2016). URL: https://spiral.imperial.ac.uk:8443/handle/10044/1/42222.